Available online at www.sciencedirect.com

SCIENCE DIRECT

Journal of Sound and Vibration 271 (2004) 615–633

JOURNAL OF SOUND AND VIBRATION

www.elsevier.com/locate/jsvi

Experiments and simulated calculations on the resistance to low-velocity impact of layered plates with a sandwiched ERM

Yinyan Zhao*, Tianyuan Xiao, Sixin Xue, Janhua Dong

Automation Department, CIMS Engineering Research Center, Tsinghua University, Haidian District, Beijing 100084, People's Republic of China

Received 13 May 2002; accepted 10 March 2003

Abstract

Comparison experiments and simulated calculations are conducted on the resistance to low-velocity (or low-energy) impact of layered structures with and without an electro-rheological material (ERM) sandwiched, under different electric voltages applied to the ERM layer. From the experiments, it is found that the stiffness of the specimen under different electric intensities applied to the ERM layer is approximately a constant. From the calculations, within the range of $0.0\,\text{kV/mm} \leqslant E \leqslant 3.5\,\text{kV/mm}$, the resistance to impact decreases somewhat with the increasing electric intensity for the layered composite specimens. The same conclusion is obtained for a layered aluminum plate within the range of $0.0\,\text{kV/mm} \leqslant E \leqslant 0.75\,\text{kV/mm}$. Meanwhile, data from the experiments and calculations show that these results are repeatable under different impact velocities. Further analysis by computations shows that the change of viscous proportional damping, $[C] = \alpha[M] + \beta[C]$, is the main cause of the reduction of the specimen's resistance to impact, where the stiffness coefficient β is the key factor.

1. Introduction

1.1. Electro-rheological materials and their mechanical properties

Electro-rheological materials (ERMs) are intelligent materials that are suspensions with polarizable solid particulates with relatively high permittivity (e.g., starch) dispersed in a non-polar carrier fluid with low electric conductivity (e.g., silicon oil). The electro-rheological effect was first discovered by Winslow in 1949. In the 1980s, ERMs attracted more attention of researchers in different areas and much development was obtained in confecting of ERMs,

---

*Corresponding author. Tel.: +86-01-62789635; fax: +86-01-62770351.

E-mail address: yinyanz@263.net (Y. Zhao).

0022-460X/03/$ - see front matter © 2003 Elsevier Ltd. All rights reserved.
doi:10.1016/S0022-460X(03)00284-0

explanation of their mechanism, property measurement and application exploration. The most important characteristics are their fast and reversible rheological properties. Their material properties, such as viscosity, stiffness and elasticity, can change drastically when subjected to a high-intensity electric field (usually, several kV/mm) and vary continuously with changes in the applied voltage. When the electric field is annulled they revert to the original state. These properties endow the products featuring ERMs with a short response time, adjustability of damping and stiffness, low-energy loss, and easy controllability by computer. ERMs development promises further applications in areas such as isolators, brakes, real-time control and electro-mechanics.

ERM can be regarded as a Newtonian fluid when the electric field intensity E applied is lower than a threshold E_c and it shows low viscosity and a very faint electro-rheological effect. When the field intensity E exceeds E_c, the viscosity of the ERM consequently increases and the ERM becomes a non-Newtonian fluid displaying characteristics similar to those of a solid [1]. The deforming mode of ERMs can be deduced as follows. Under static shear, before yielding, the behavior of an ERM is similar to that of a solid. While yielding, it can be regarded as a Binham fluid [2–4]; under non-static shear and a periodic load of moderate frequency, the behavior of an ERM can be described as that of a visco-elastic or a visco-elastic and visco-plastic material. Usually, an ERM is characterized concurrently by viscosity, elasticity and plasticity. Its dominant properties change with the intensity change of the applied electric field [2].

The micro-mechanism of electro-rheological effect is now known and the microstructure of ERMs under electric fields is made up of many small crossed or paralleled chains, formed by particles aligned along the field lines, and viscous liquid filled around the chains. Then, the mechanical property along the field lines can be macroscopically simulated with a group of small springs and dampers. The property normal to the electric field can be analogously simulated with shear springs and dampers along the shear direction [5].

Some mechanical models of ERMs under dynamic loading have been put forward individually as concrete research objects, which often consist of several viscous elements, Coulomb or frictional and elastic elements [2,6].

1.2. Research on adaptive structures featuring ERMs

Various intelligent products with ERMs as their actuators and control materials are being developed. Some of these products include clutches, brakes, shock absorbers, vibration isolators, adaptive structures, dampers, and valves.

Two main effects of ERMs exist in structures [5]. One effect is to restrain the relative motions along the direction normal to the electric field inside the ERM or between the ERM and the electrodes. The other effect is to change the amplitudes, frequencies, and phases of the dynamic responses of the structures along the direction parallel to the electric field, by changing the viscosity, or stiffness of the ERM. Correspondingly, products featuring ERMs can be divided into two groups according to the above two kinds of ERM effect in structures. Most of the products are from the application of the former effect, such as dampers, shock absorbers, and clutches. Work on these has been published in various media [7–10]. Studies on the application of the latter effect are relatively few, only restricted to vibration isolators and adaptive structures.

An adaptive beam is a typical adaptive structure utilized by researchers. Yalcintas, Coulter and Dai in 1998 and 1999 discussed the vibration minimization capabilities of ERM adaptive beams simply supported at the two ends under different conditions [11,12]. Yalcintas and Coulter conducted research on the modelling of the adaptive beam structures with various boundary conditions. Sprecher et al. utilized an ERM as the inner layer in sandwich structures of composite plates and did some work on the vibration control of an adaptive cantilever in 1990 and 1991 [13]. Apart from these adaptive beams, other forms of adaptive structures featuring ERMs have been seldom studied. Furthermore, their loadings are limited to sinusoidal stimuli at single or multiple points. However, in real applications, different loadings and various structures often exist, among which impact load is a typical one and the square-layered plate with four sides clamped is a good representation of many real structures. The dynamic behavior of the layered adaptive structures under an arbitrary impact load has not yet been touched upon in literature.

As we know, composite structures are widely used in aerospace engineering. However, there exists a distinct shortcoming in them, namely, their low resistance to impact. Carbon-fiber laminated composite plate is a typical composite material. That is why it is selected as one object material. Aluminum alloy is also a typical engineering material and is often exposed to unexpected impact loading. It is also a good conductor and can be used as an electrode. So it is selected as another object material.

In addition, three kinetic modes have been summarized according to the deformation types of ERMs under external loadings [5], which are shear mode, flow mode and press–pull mode. These refer to the state only shear stress acts, only damp forces act and only compressive or tensional stresses act, respectively. These three modes can occur alone or in combination, depending on practical conditions. In most cases, shear mode plays the main role. In the investigation referred to in this paper, the press–pull effect is ignored and the shear effect and the flow effect occur in combination, which is determined by the structure of the specimen, the constraint and the load applied to it.

In this study, the structure's resistance change with impact is investigated before and after an ERM layer is sandwiched. Strain and deflection are measured and calculated under different cases. The results from experiments are compared with those from calculations, which are based on a model established and validated by the finite element method (FEM) in Ref. [5].

2. Experiments

Experiments in this study, static tests and low-velocity or low-energy impact tests are conducted. The density of electro-rheological suspension used is $\rho = 1.047\,\mathrm{g/cm^3}$. The mass ratio of solid particles (dispersant) to insulating oil (dispersoid), the two main ingredients of the ERM, is 0.648.

2.1. Specimens

The specimens are 200 mm × 200 mm layered plates with its four sides clamped. Fig. 1 is the sketch of the structure, where load F refers to the contact force during impact. Four specimens are

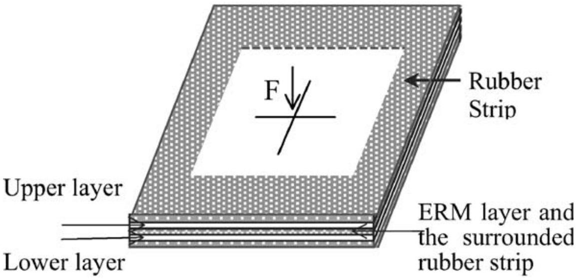

Fig. 1. Sketch of the specimen used in the experiments.

designed and listed as follows. Specimens #1 and #2 are three-layered plates with the ERM as the middle layer. Specimens #3 and #4 are corresponding two-layered plates without an ERM layer.

Specimen #1: A three-layered plate with the ERM as the middle layer and C-fiber laminated composite material plates as the upper and the lower layers. The thickness of each layer is 1 mm. The material data are as follows.

Model: T300/QY8911; layer type $(0^\circ/45^\circ/-45^\circ/90^\circ)_8$; the parameters of a single layer; Thickness $h = 0.125\,\text{mm}$; density $\rho = 1614\,\text{kg/m}^3$; Young's modulus $E_1 = 135\,\text{GPa}$, $E_2 = E_3 = 8.8\,\text{GPa}$; shear modulus $G_{12} = G_{13} = 4.47\,\text{GPa}$; the Poisson ratio $\upsilon_{12} = \upsilon_{13} = 0.33$.

Specimen #2: A three-layered plate with the 2 mm thick ERM as the middle layer and aluminum plates as the upper and the lower layers, whose thicknesses are 0.5 and 2 mm, respectively. Their material data are as follows.

The upper plate: Model: LY12CZ. Property parameters: $\rho = 2800\,\text{kg/m}^3$, $E = 68\,\text{GPa}$, $G = 26\,\text{GPa}$, $\upsilon = 0.33$ The lower plate: Model: LF21M. Property parameters: $\rho = 2730\,\text{kg/m}^3$, $E = 70\,\text{GPa}$, $G = 27\,\text{GPa}$, $\upsilon = 0.296$.

Specimen #3: A two-layered C-fiber laminated composite square plate. It is made of an upper layer and a lower layer as in specimen 1#.

Specimen #4: A two-layered aluminum square plate. It is made of an upper layer and a lower layer as in specimen 2#.

For specimens 2# and 4# utilized in experiments, in view of the need to isolate the aluminum plates, namely, the two electrodes, and to seal the ERM layer, some rubber strips are inserted at the surrounding fringe of the plates between the upper and lower aluminum plates and also between the plates and the clamper.

In the experiments, strain gauges are distributed on the lower surface of the specimen, as sketched in Fig. 2. Gauges 1, 2, 3 and 4 are located along the direction of 45° and gauges 5, 6, 7 and 8 are along the direction of 0°, parallel to one side of the specimen.

2.2. Static experiment

A general static pressure experiment is conducted.

Main equipment and instruments include CSS-1110 multi-functional electronic test machine, static strain gauge, power resource with high voltages (scope 6 kV), and strain gauge flake with a resistance range of $120 \pm 1\,\Omega$. The content is to measure the force and the strain of specimens #2 and #4 under different electric voltages applied to the ERM layers. Parameters to be measured

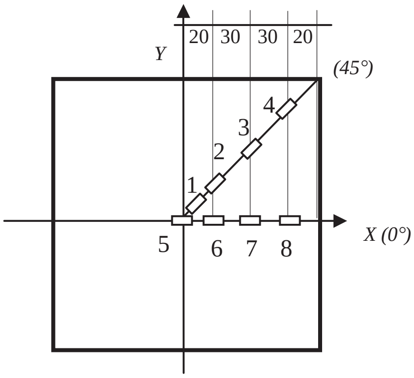

Fig. 2. Position of the strain gauges on the lower surface of the specimen.

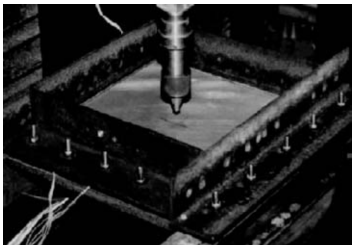

Fig. 3. Photograph of a specimen before experiment.

include forces applied to the center of the plate and the gauge values while the force is being applied.

A picture of the clamped specimen with ERM is shown in Fig. 3.

Fig. 4 shows smoothed lines of force F versus the corresponding strain for intensity E equals to 0.0, 0.3, 0.5, 1.0, 1.2 kV/mm, respectively. The thicker line corresponds to the case of no ERM sandwiched between the plates (specimen #4). The smoothed linear expression is $\Delta F = k\Delta\varepsilon$, where the unit of F is Newton and ε is dimensionless. Values of the slope k are listed in Table 1. It can be said that the slope for the specimen without an ERM is a little smaller than those for the specimen with the ERM (#2). The slope differences for a specimen with the ERM under different voltages are very small and within the range of 6.3%, and the average relationship is: $\Delta F = 217.7\Delta\varepsilon$. Hence the stiffness of a specimen with the ERM can be approximately regarded as a constant and not affected by the applied electric voltages.

2.3. Low-velocity impact experiment

Free falling experiment with low-energy or low-velocity impact is conducted.

Main equipment and instruments include TDS540A digital oscillograph and YJD dynamic strain gauge. The content is to measure the real-time response curves of specimens #2 and #4 under different voltages and different velocities. Parameters to be measured include impact velocities, applied electric field intensities and strain responses.

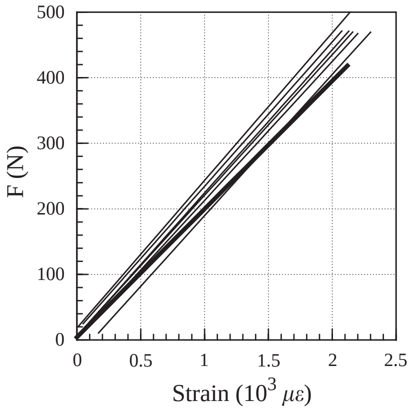

Fig. 4. Fitted lines of force F versus strain ε_0 for specimens #2 and #4. The thicker one is for specimen #4 (without ERM).

Table 1
Slopes of fitted $F - \varepsilon_0$ lines under static loading

Cases	No ERM	Electric intensity applied to ERM E (kV/mm)						
		0.0	0.3	0.5	0.75	1.0	1.2	Average
Slop $k(\times 10^3)$	195.5	212.1	214.7	220.3	225.3	218.3	215.4	217.7

The shape and the size of the impactor are shown in Fig. 5, whose mass is $m = 145.5$ g; density: $\rho = 7.8\ \mathrm{g/cm^3}$; Young's modulus: $E = 200$ GPa; shear modulus: $G = 81$ GPa; the Poisson ratio: $\upsilon = 0.29$.

2.3.1. Experimental results and analysis

Figs. 6(a) and (b) show the time–strain response curves from the eight gauge flakes stuck on the lower surface of specimens #2 and #4, under the impact velocity of 2.95 m/s. It can be seen from the plots that their strain amplitudes are reduced gradually as their distance increases from the center of the plate, and the amplitude reduction becomes acute at around 50 mm away from the center. Meanwhile, apart from the strain on flakes 5 and 1, other strains show negative at the starting time and the negative phase becomes wider as the distance between the flake and the center increases. The vibration wave shape of the plate caused by the impact can be constructed from the eight gauge values.

Fig. 7 shows the real time–strain responses of aluminum specimens, specimens #2 and #4, at the electric field intensities of 0.0, 0.25, 0.50, and 0.75 kV/mm and at the impact speeds of 1.80, 2.36, 2.95, and 3.55 m/s, individually. The strain refers to the one of flake 5, which is along the 0° at the center of the lower surface of the specimen and can be named as ε_0. The first column in the figure is the plots for specimen #4 (without an ERM) and the second column is plots for specimen #2 under zero electric intensity (no electric voltage applied). Comparing the plots without ERM with those with ERM, but with no electric voltage applied, it can be concluded that almost all strain

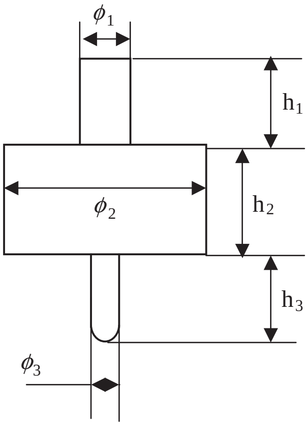

Fig. 5. Size and shape of the impactor, $h_1 = h_2 = h_3 = 20\,\text{mm}$, $\phi_1 = 12\,\text{mm}$, $\phi_2 = 31.7\,\text{mm}$, and $\phi_3 = 6\,\text{mm}$.

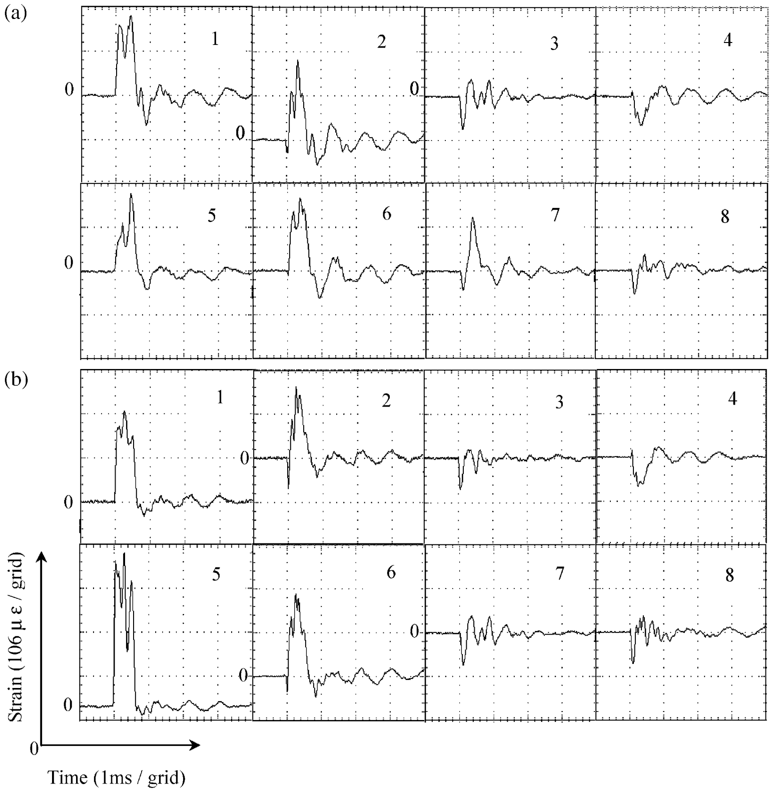

Fig. 6. (a), (b) Measured strain responses of the gauge flakes on specimen #2 and specimen #4, respectively, under impact velocity of 2.95 m/s.

and deflection responses of the specimen, after sandwiching ERM, are reduced considerably. The main reason is the increasing damping of the structure as analyses in the following section. By comparing the plots for the specimens with an ERM in the right four columns in Fig. 7, it

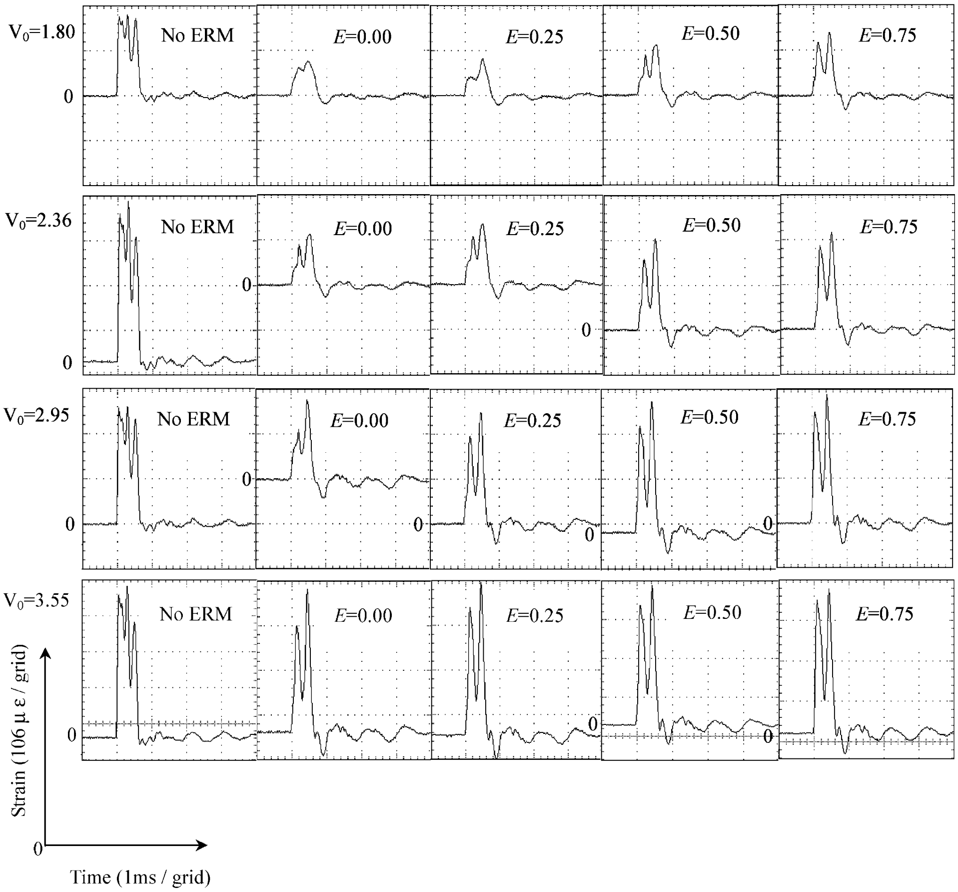

Fig. 7. Measured strain responses of flake 5 at the lower surface of specimen #4 (no ERM) and #2(with ERM) at four sample electric intensities applied to the ERM layer, 0.0, 0.25, 0.5, and 0.75 kV/mm, under impact velocities of 1.80, 2.36, 2.95, and 3.55 m/s.

can be observed clearly that the responses featuring an ERM increase with the increase of the applied electric intensities. These results remained consistent for different impact velocities. These results also agree well with the results from calculations, which are presented in later sections.

The peak strain values of the above plots are listed in Table 2 and plotted in Fig. 8 versus the electric intensity. That the strain amplitudes increase with the intensity increase can be observed clearly. It should be explained that only the first-class frequency wave is considered in view of the research goal of this paper, and the data in Table 2 and Fig. 8 are from the smoothed strain curves, in which high-frequency waves are discarded. In addition, as can be observed from any single plot in Fig. 7, the amplitude of a high-class wave is enlarged, which is probably because its frequency is close to the nature frequency of the system.

Summarizing the above, from the dynamic experiments, in the electric intensity range of 0.0 kV/mm$\leqslant E \leqslant$0.75 kV/mm, although the resistance of the aluminum layered plate to impact is

Table 2
Experimental results of the strain responses amplitudes ($\mu\varepsilon$) for specimen with ERM (#2) at the sample electric intensities under different impact velocities

Impact velocities v_0 (m/s)	Electric intensity applied to ERM E (kV/mm)			
	0.0	0.25	0.5	0.75
1.80	345.3	369.9	389.5	504.7
2.36	389.5	522.4	672.8	725.8
2.95	610.9	832.2	920.5	973.6
3.55	1027	1098	1168	1179

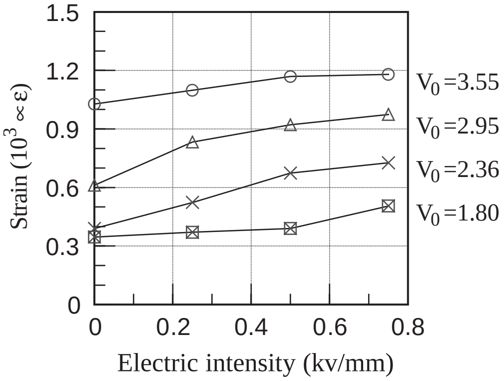

Fig. 8. Measured strain amplitudes of ε_0 varying with electric intensity on specimen #2 under different impact velocities.

enhanced markedly after an ERM is inserted as a middle layer, the impact resistance of the plate with an ERM inserted decreases with the electric intensity increase.

3. Simulated calculations

3.1. Modelling of the layered plate with a sandwiched ERM

The modelling by the FEM of the layered structure with the ERM sandwiched, under low-velocity impact load, was discussed and validated specifically in Ref. [5], which will be mentioned here briefly. Meanwhile, some key functions and equations in the establishment of the FEM model are given here in detail.

A quarter of the plate is chosen by virtue of the symmetry of the structure, and it is divided into 31 eight-node isoparametric layered elements, as sketched in Fig. 9.

Modelling by the FEM is based on the following three assumptions:

(1) Under small deformation, the normal line vertical to the element mid-surface before deformation remains a straight line after deformation.

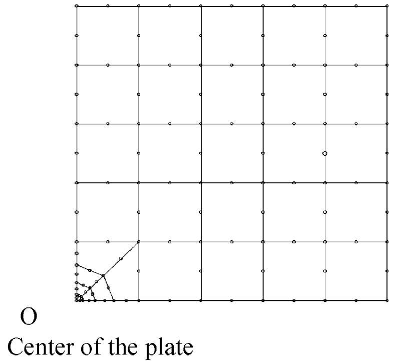

Fig. 9. Net division in 1/4 of the plate.

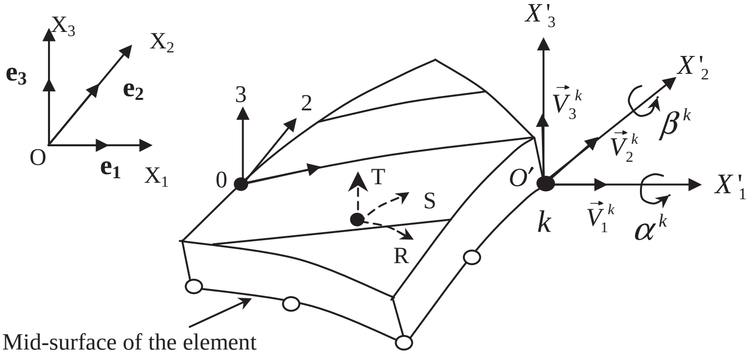

Fig. 10. Four reference coordinate systems, $(OX_1X_2X_3)$ is a global coordinate system; (RST) is a natural coordinate system; $(OX_1'X_2'X_3')$ is a local system and (0123) is an elasticity main axis system.

(2) No normal stress exists in the plate, perpendicular to the mid-surface.
(3) There is no slipping between layers.

Then the element discussed here in three dimensions is turned into a two-dimensional element.

According to the features of the structure and the deformation of the specimens, 4 reference coordinate systems are established, which are shown in Fig. 10. $(OX_1X_2X_3)$ is a general (or global) coordinate system with O at the plate center and axes X_1 and X_2 that are parallel, respectively, to the adjacent two sides of the square plate; that is to say that OX_1X_2 plane is coplanar with the mid-plane of the plate before deformation. $\mathbf{e}_1$, $\mathbf{e}_2$, $\mathbf{e}_3$ are the corresponding unit vectors of the three axes, respectively; (RST) is a natural coordinate system within an element with the origin at the center of the element mid-surface. R and S are coordinates at the mid-surface and T is the line coordinate along the vertical direction of the mid-surface; $(O'X_1'X_2'X_3')$ is a local coordinate system with the origin at node k. Axis X_3' is along the direction of the mid-surface normal line and X_1' is vertical to axis X_2 in the global system. $\vec{V}_1^k$, $\vec{V}_2^k$, and $\vec{V}_3^k$ are the corresponding unit vectors of the three axes, respectively. Before deformation, the relationships between the general system, the natural system and the local system are only line displacements with no rotations.

(0123) is an elasticity main axis coordinate system with the origin at a random point j in one layer of the plate. Axis 01 is along the longitudinal direction of the fiber in a composite material layer and axis 03 is along the vertical direction of the fiber.

An eight-node isoparametric layered shell element is based on the eight-node isoparametric element and consists of several layers superposed. For a point in the plate, there are 5 independent freedoms, in which 3 are line displacements in the general coordinate system, which are u_1, u_2 and u_3; and 2 are rotation displacements in the local systems, which are α and β. The two rotation displacements are formed by vector $\vec{V}_3$ rotating around $\vec{V}_1$ and $\vec{V}_2$, respectively.

The shape function of node k in the general system is N_k, which is the same as that of the plane eight-node isoparametric element, as follows:

$$\begin{gathered}N_1 = \tfrac{1}{4}RP*SP - \tfrac{1}{2}N_5 - \tfrac{1}{2}N_8, \quad N_2 = \tfrac{1}{4}RM*SP - \tfrac{1}{2}N_5 - \tfrac{1}{2}N_6, \\ N_3 = \tfrac{1}{4}RM*SM - \tfrac{1}{2}N_6 - \tfrac{1}{2}N_7, \quad N_4 = \tfrac{1}{4}RP*SM - \tfrac{1}{2}N_7 - \tfrac{1}{2}N_8, \\ N_5 = \tfrac{1}{2}R2*SP, \quad N_6 = \tfrac{1}{2}RM*S2, \quad N_7 = \tfrac{1}{2}R2*SM, \quad N_8 = \tfrac{1}{2}RP*S2,\end{gathered} \tag{1}$$

in which

$$RP = 1.0 + R, \quad RM = 1.0 - R, \quad SP = 1.0 + S$$

and

$$SM = 1.0 - S, \quad R2 = 1.0 - R^2, \quad S2 = 1.0 - S^2.$$

Displacement mode and general coordinates of point j, one random point in an eight-node isoparametric layered shell element, are as follows:

$$u_i = \sum_{k=1}^{M} N_k u_i^k + \frac{\bar{h}_j}{h_j}\sum_{k=1}^{M} N_k h_k(-\alpha^k V_{2i}^k + \beta^k V_{1i}^k) \quad (i = 1,2,3), \tag{2}$$

$$X_i = \sum_{k=1}^{M} N_k X_i^k + \frac{\bar{h}_j}{h_j}\sum_{k=1}^{M} N_k h_k V_{3i}^k \quad (i = 1,2,3), \tag{3}$$

where $M = 8$ is the node number in the mid-surface of the shell element, u_i^k is the displacement of node k in X_i $(i = 1,2,3)$ direction, X_i^k the coordinate of node k in X_i $(i = 1,2,3)$ direction in the general system, V_{si}^k the direction cosine of vector V_s^k $(s = 1,2,3)$ at node k in X_i $(i = 1,2,3)$ direction in the general system, h_k the thickness along the normal line of mid-surface passing point k, h_j the thickness along the normal line of mid-surface passing point j, $\bar{h}_j$ the vertical distance from point j to the mid-surface.

From the above shape function and displacement mode, the geometry matrix $[B]$ and displacement–strain relation $\{\varepsilon\} = [B]\{u\}$ can then be deduced.

The displacement–strain relation of a single layer in the main axis system is expressed as

$$\{\sigma_{123}\} = [C]\{\varepsilon_{123}\}, \tag{4}$$

where

$$[C] = \begin{bmatrix} C_{11} & C_{12} & C_{13} & 0 & 0 & 0 \\ C_{12} & C_{22} & C_{23} & 0 & 0 & 0 \\ C_{13} & C_{23} & C_{33} & 0 & 0 & 0 \\ 0 & 0 & 0 & C_{44} & 0 & 0 \\ 0 & 0 & 0 & 0 & C_{55} & 0 \\ 0 & 0 & 0 & 0 & 0 & C_{66} \end{bmatrix} \tag{5}$$

is the elasticity modulus matrix in the main axes system, in which

$$C_{11} = \frac{E_1(1-\upsilon_{23}\upsilon_{32})}{\upsilon}, \quad C_{12} = \frac{E_2(\upsilon_{12}+\upsilon_{32}\upsilon_{13})}{\upsilon}, \quad C_{13} = \frac{E_3(\upsilon_{13}+\upsilon_{12}\upsilon_{23})}{\upsilon},$$
$$C_{22} = \frac{E_2(1-\upsilon_{13}\upsilon_{31})}{\upsilon}, \quad C_{23} = \frac{E_3(\upsilon_{23}+\upsilon_{21}\upsilon_{13})}{\upsilon}, \quad C_{33} = \frac{E_3(1-\upsilon_{12}\upsilon_{21})}{\upsilon},$$
$$C_{44} = G_{12}, \quad C_{55} = G_{23}, \quad C_{66} = G_{31},$$

and where E_i is the elasticity Young's modulus in axis $i(=1,2,3)$; υ_{ij} the Poisson ratio; G_{ij} the shear modulus in ij plane; $\upsilon = 1-\upsilon_{12}\upsilon_{21}-\upsilon_{23}\upsilon_{32}-\upsilon_{13}\upsilon_{31}-2\upsilon_{21}\upsilon_{32}\upsilon_{13}$ and $\upsilon_{ij}/E_i = \upsilon_{ji}/E_j$, $i,j = 1,2,3$.

If $[Q]$ is the transformation matrix between the main axes system and the local system, the elasticity modulus matrix $[C']$ in the local system is expressed as

$$[C'] = [Q]^{\mathrm{T}}\cdot[C]\cdot[Q]. \tag{6}$$

According to assumption (2), the stress in X_3' direction in the local system is $\sigma_3' = 0$. Hence, the matrix $[C']_{6\times6}$ can be condensed to $[\tilde{C}]_{5\times5}$.

The transformation matrix between the local system and the general system can be obtained as well when their position relation is known. The condensed matrix is $[T]_{5\times6}$ and the elasticity modulus matrix is

$$[D] = [T]^{\mathrm{T}}\cdot[\tilde{C}]\cdot[T]. \tag{7}$$

After $[D]$ is determined, the stress state of a point in an element in the general system can be determined eventually: $\{\sigma\} = [D]\{\varepsilon\}$.

In the general system, the initial displacements and coordinate values of a point are

$$u|_{t=0} = \begin{Bmatrix} X_{10} \\ X_{20} \\ X_{30} \\ 0 \\ 0 \end{Bmatrix}, \quad X_{i0} = \sum_{k=1}^{8} N_k X_{i0}^k, \quad i = 1,2,3, \tag{8}$$

where X_{i0}^k is the initial coordinate values of node k.

The boundary displacement constraint condition of the plate with four sides clamped is

$$\begin{Bmatrix} u_1 \\ u_2 \\ u_3 \\ \alpha \\ \beta \end{Bmatrix}_{X_1=\pm a} = \begin{Bmatrix} 0 \\ 0 \\ 0 \\ 0 \\ \beta \end{Bmatrix}, \quad \begin{Bmatrix} u_1 \\ u_2 \\ u_3 \\ \alpha \\ \beta \end{Bmatrix}_{X_2=\pm a} = \begin{Bmatrix} 0 \\ 0 \\ 0 \\ \alpha \\ 0 \end{Bmatrix}, \tag{9}$$

where a is the half-side width of the square plate.

The motion equation of the impact system, which consists of the goal plate and the impactor, is listed in expression (10), where, $[M]$, $[K]$, and $[C]$ are the mass matrix, the stiffness matrix and the damping matrix, respectively; $\{R\}$ is the load column; $\{u\}$, $\{\dot{u}\}$ and $\{\ddot{u}\}$ are the displacement, the velocity and the acceleration columns, respectively.

$$[M] \cdot \{\ddot{u}\} + [C] \cdot \{\dot{u}\} + [K]\{u\} = \{R\}. \tag{10}$$

The mass matrix and the stiffness matrix of the system are determined after the material parameters of the ERM have been obtained by measurement and the Gauss coordinate expressions of each layer of the structure have been deduced. During contact, the total mass of the system is made up of the plate mass and the impactor mass added to the central area of the plate. The system damping is simulated by viscous proportional damping to consider the linear viscous and elastic damping shown by the ERM under the small deformation hypothesis. The concrete expression is: $[C]=\alpha[M]+\beta[C]$, where α and β are proportional damp coefficients. When simulating the contact force during impact, the force is simulated by the prediction method [14] and the modified prediction method [15] for the composite layered plate and the aluminum plate, respectively.

In practical calculations, the ERM under electric voltage can be approximately treated as isotropic.

The equation was carried out by the Newmark direct integration method.

3.2. Calculation results and discussion

3.2.1. Dynamic responses of a layered aluminum plate with a sandwiched ERM

Specimens #4 and #2 are used here again for response calculations. All conditions and parameters are same as those in the experiments. Impactor mass: $m = 145.5\,\mathrm{g}$. Impact velocities: $v_0 = 1.80$, 2.36, 2.95, 3.55 m/s. Electric intensity range: $0.0\,\mathrm{kV/mm} \leqslant E \leqslant 0.75\,\mathrm{kV/mm}$, and four sample values: $E = 0.0$, 0.25, 0.5, and 0.75 kV/mm are chosen.

Calculated values of strain ε_0 are plotted in Fig. 11 with the increase of the applied qelectric intensity. Experimental results corresponding to different impact velocities are shown in Fig. 7. The plots in Fig. 11 show that the trend of the strain remains identical for different velocities.

Strain and deflection amplitudes with electric intensity are shown in Figs. 12(a) and (b), respectively. The same trend of the responses of the system increasing with the increase of the applied electric intensity as observed in the above experiments, can be seen here. The corresponding data are listed in Tables 3 and 4, respectively. The increase of the deflection

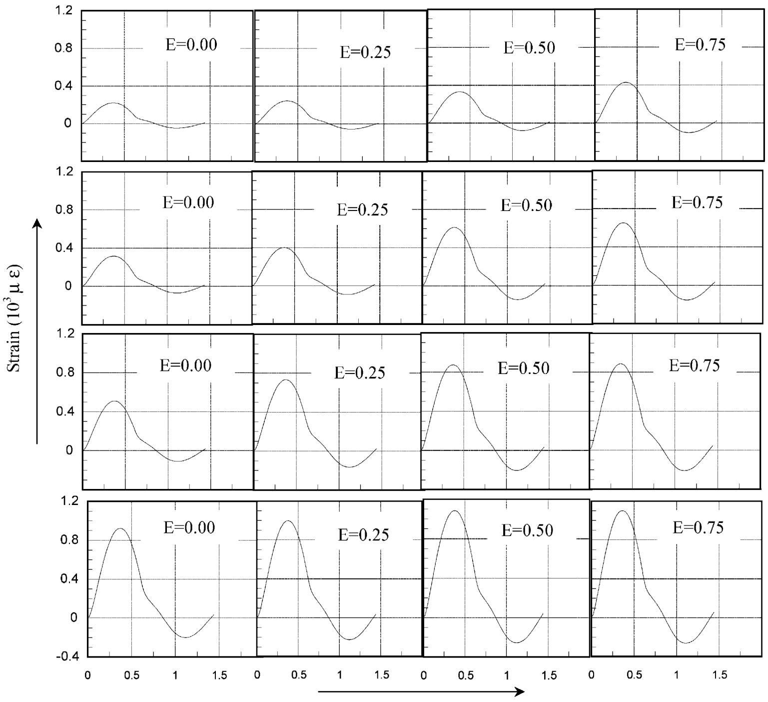

Fig. 11. Calculated strain responses of flake 5 at the center of the lower surface of #2 (with ERM) at four sample electric intensities, 0.0, 0.25, 0.5, and 0.75 kV/mm, under different impact velocities of 1.80, 2.36, 2.95, and 3.55 m/s.

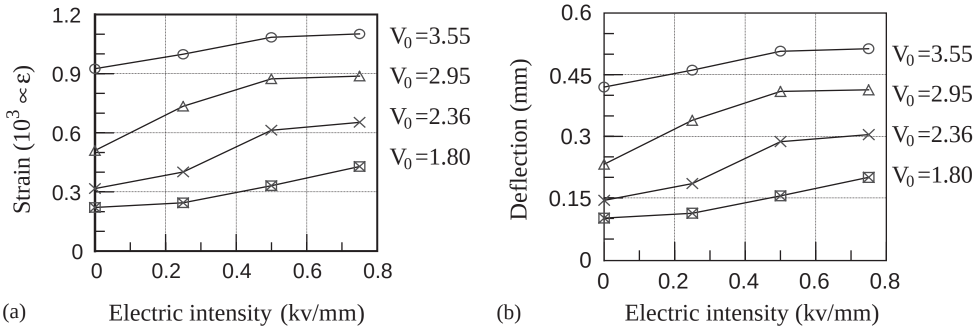

Fig. 12. (a), (b) Calculated strain and deflection amplitudes of ε_0 and D_0 varying with electric intensity on specimen #2 under different impact velocities.

amplitude induced by the intensity increase is within the range of 10–20% and that of the strain is within the range of 13–106%.

By comparing the curves in Figs. 11, 12(a), 7 and 8, it can be concluded that there is an identical varying trend between the strain curves from experiments and calculations for each velocity. The strain errors between the data from experiments and calculations are listed in Table 5, most of

Table 3
Calculated strain amplitudes of ε_0 on specimen #2 varying with electric intensity under different impact velocities

Impact velocities v_0 (m/s)	Electric intensities applied to ERM (kV/mm)			
	0.0	0.25	0.5	0.75
1.80	221.3	244.6	331.4	428.4
2.36	317.5	401.1	612.5	652.5
2.95	509.1	733.9	873.4	887.2
3.55	923.7	997.9	1084	1101

Table 4
Calculated deflection amplitudes of D_0 on specimen #2 varying with electric intensity under different impact velocities

Impact velocities v_0 (m/s)	Electric intensities applied to ERM (kV/mm)			
	0.0	0.25	0.5	0.75
1.80	0.101	0.113	0.155	0.2
2.36	0.144	0.185	0.287	0.304
2.95	0.232	0.339	0.409	0.413
3.55	0.42	0.461	0.507	0.513

Table 5
Errors between the calculated and experimental results of strain ε_0 (%)

Impact velocities v_0 (m/s)	Electric intensities applied to ERM (kV/mm)			
	0.0	0.25	0.5	0.75
1.80	−35.9	−33.9	−14.9	−15.1
2.36	−18.5	−23.2	−8.96	−10.1
2.95	−16.7	−11.8	−5.12	−8.87
3.55	−10.1	−9.12	−7.19	−6.62

which are within the range of 5–20%. Given the complexity, the difficulty of the experiments under high voltages and the novelty of testing a dynamic response under low-velocity impact for layered plates featuring an ERM, the errors are regarded as reasonable and acceptable. It can be concluded that the results from the experiments and the calculations agree well.

3.2.2. Dynamic responses of a layered composite plate with a sandwiched ERM

Specimen #1 is used here as another calculation example. Impact condition: Impactor mass: $m = 50\,\text{g}$; impact velocity: $v_0 = 2.0\,\text{m/s}$; electric intensity range: $0.0\,\text{kV/mm} \leqslant E \leqslant 3.5\,\text{kV/mm}$, and eight sample values: $E = 0.0$, 0.5, 1.0, 1.5, 2.0, 2.5, 3.0, and 3.5 kV/mm are chosen. The deflection and the strain responses of the specimen under different electric intensities are calculated here.

The deflection surface of the specimen at maximum deformation varying with the electric intensity is shown in Fig. 13 and the deflection curve of the center point versus the intensity at different times is shown in Fig. 14(a). From these two figures, it can be deduced that the responses or the energy absorbency of the plate featuring an ERM increases with an increase in electric intensity, especially when it exceeds 1.0 kV/mm. Meanwhile, the course of deflection D_0 and strain

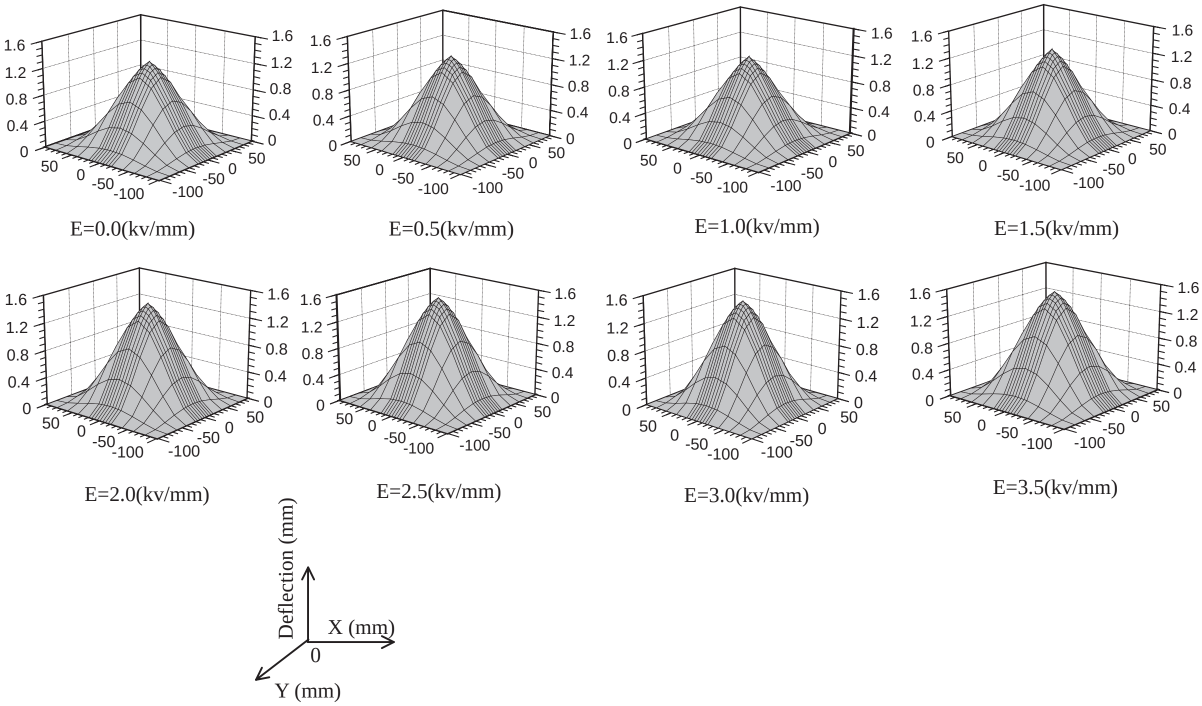
E=0.0(kv/mm) E=0.5(kv/mm) E=1.0(kv/mm) E=1.5(kv/mm)

E=2.0(kv/mm) E=2.5(kv/mm) E=3.0(kv/mm) E=3.5(kv/mm)

Fig. 13. Deflection surfaces of the specimen at maximum deformation varying with the electric intensity.

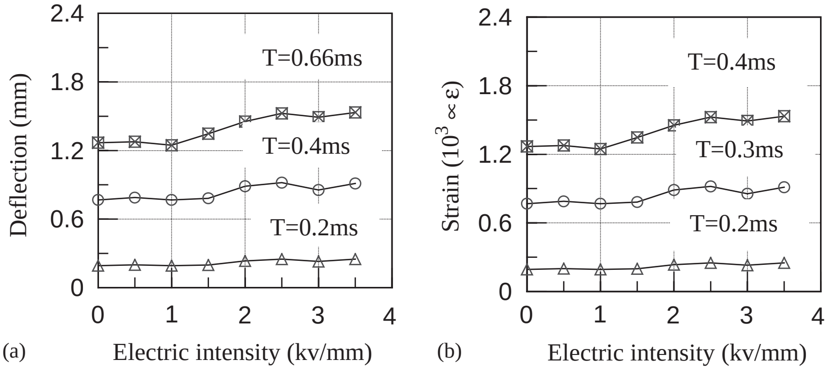

Fig. 14. (a), (b) Deflection D_0 and strain ε_0 on specimen #1 varying with electric intensity at different times. Damping is included.

ε_0 varying with intensity E are traced and the curves at three times are shown in Figs. 14(a) and (b). The results show that when the electric intensity reaches the maximal value, 3.5 kV/mm, the deflection increases 29.9%, 19.8% and 22.6% at the times $T = 0.2$, 0.4, and 0.66 ms, respectively. The strain increases 9.3%, 36.0%, and 55.0% at the times $T = 0.2$, 0.3, and 0.54 ms, respectively. Also, it can be observed that the peak of the strain occurs earlier than that of the deflection; the former is 0.54 ms and the latter is 0.66 ms.

It can be concluded from these calculations for specimen #1 that the resistance to impact does not show obvious waving when $E < 1.0$ kV/mm and is lowered with the increase of the electric intensity increase when $E > 1.0$ kV/mm. This result is identically reproduced when the impactor mass and the impact velocity change. It agrees with the results for specimen #2.

3.3. Discussion

For form (10), when the design and the construction of a system is finished, mass M will be a constant, but stiffness K and damping C will vary with the change of the property parameters of the ERM, which is caused by the change of the applied electric voltage. So, the responses of the impact system are related closely to the comprehensive change of stiffness K and damping C. In order to clarify which is the main contributor or how to divide the responses' change, first, only the stiffness is considered in the equation and the damping item in form (10), $[C]$ is discarded. Then the corresponding response calculations are conducted on specimen #1 under the same impact velocities and the electric intensity range as before. The results are compared with those obtained in Section 3.2.2, in which both stiffness K and the damping C are considered in the model equation together.

In Figs. 15(a) and (b) are the curves of deflection D_0 and strain ε_0 versus intensity E at three time points, respectively. The deflection is at $T = 0.2$, 0.4, and 0.66 ms, in which 0.66 ms corresponds to the maximum situation. The strain is obtained at $T = 0.2$, 0.3, 0.4 ms, in which 0.4 ms corresponds to the maximum situation. From these curves, it can be seen that when damping is discarded, the deflection and the strain decrease slightly. That is to say, the stiffness change brings a very faint effect to the dynamic response of the system. While in Fig. 14 when the

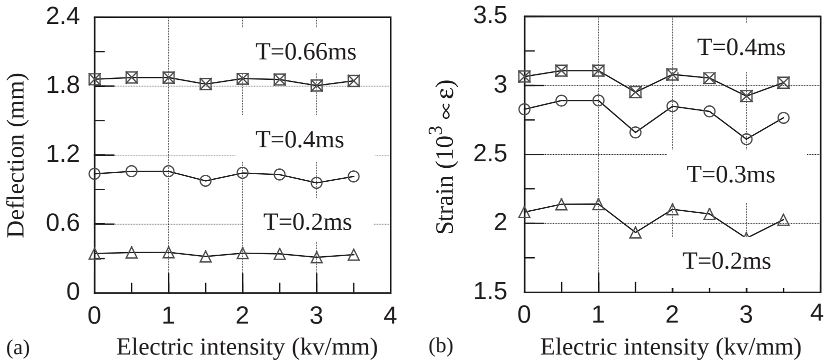

Fig. 15. (a), (b) Deflection D_0 and strain ε_0 on specimen #1 varying with electric intensity at different times. No damping is included.

damping is taken into account, the dynamic responses show an obvious rising trend. So the decrease of the pure viscous damping brings a primary effect to the increase of the responses, or decreases the system's resistance to impact.

In the assumption of viscous proportional damping, $[C] = \alpha[M] + \beta[K]$, with the applied electric intensity increasing, $\alpha[M]$ also increases because the coefficient α increases and $[M]$ is a constant [5]. Then the damping decrease is mainly caused by the decrease of the stiffness proportion damping $\beta[K]$. Meanwhile, the static experiments show that the stiffness hardly changes with the applied voltages. So the damping decrease is finally caused by the decrease of stiffness proportion coefficient, β, in the condition that the dynamic stiffness and static stiffness of the ERM is approximately the same.

4. Conclusion

Conclusions from the above sections on the experiments and calculations can be summarized briefly. For the ERM sandwich plate utilized in this paper, under low-velocity impact, the dynamic responses increase with the increase of the applied electric intensity and the resistance to low-velocity impact decreases.

Through the experiments, calculations, comparisons and analyses, the preliminary conclusion can be drawn that for the ERM and specimen in this paper, the resistance of the ERM sandwich plate to the low-velocity or low-energy impact decreases somewhat. And the main reason is the decrease of the system damping, which is caused directly by the decrease of the stiffness proportional coefficient.

The dynamic properties of layered structures composed of intelligent material, especially the resistance property to impact load, are under study.

References

[1] Z.P. Shulman, E.V. Korobko, Yu.G. Yanovskii, The mechanism of the viscoelastic behavior of electrorheological suspensions, Journal of Non-Newtonian Fluid Mechanics 33 (1989) 181–196.

[2] D.R. Gamota, F.E. Filisko, Dynamic mechanical studies of electro-rheological materials: moderate frequencies, Journal of Rheology 35 (3) (1991) 399–463.

[3] H. Block, J.P. Kelly, Electro-rheology, Journal of Applied Physics 21 (1998) 1661–1677.

[4] W.S. Yen, P.J. Achron, A study of the dynamic behavior of an electrorheological fluid, Journal of Rheology 35 (1991) 1375–1384.

[5] Y. Zhao, T. Xiao, J. Zhao, The modeling of layered plates featuring electro-rheological material layer and its numerical and experimental validations, Aerospace Science and Technology 6 (2002) 53–62.

[6] R. Stanway, J. Sproston, R. Firoozian, Identification of the damping law of an electro-rheological fluid: a sequential filtering approach, Journal of Dynamic Systems Measurements and Control 111 (1989) 91–96.

[7] C.W. Van Nostrand, J.D. Inman, Finite element model for active constrained layer damping, active materials and smart structures, SPIE 2427 (1995) 124–139.

[8] G.Z. Yao, G. Meng, T. Fang, Parameter estimation and damping performance of electro-rheological dampers, Journal of Sound and Vibration 204 (4) (1997) 575–584.

[9] M.N. Wereley, Li. Pang, Nondimensional analysis of semi-active electrorheological and magnetorheological dampers using approximate parallel plate models, Smart Materials and Structures 7 (1998) 732–743.

[10] J.E. Lindler, N.M. Wereley, Double adjustable shock absorbers using electrorheological fluid, Journal of Intelligent Material Systems and Structures 10 (1999) 652–657.

[11] M. Yalcintas, P.J. Coulter, Electrorheological material based non-homogeneous adaptive beams, Smart Materials and Structures 7 (1998) 128–143.

[12] M. Yalcintas, H. Dai, Magnetorheological and electrorheological materials in adaptive structures and their performance comparison, Smart Materials and Structures 8 (1999) 560–573.

[13] A.F. Sprecher, Y. Choi, H. Conrad, Mechanical behavior of ER fluid-filled composites in forced oscillation, in: US/Japan Conference on Adaptive Structures, Session E, November 13–15, 1991, pp. 560–579.

[14] I.H. Choi, C.S. Hong, New approach for simple prediction of impact force history on composite laminates, American Institute of Aeronautics and Astronautics Journal 32 (10) (1994) 2067–2075.

[15] Y. Zhao, J. Jiang, T. Xiao, A new method for simulating contact force based on static strain equivalence hypothesis, Journal of Sound and Vibration 251 (5) (2002) 859–873.